Acta Crystallographica Section D
Biological Crystallography
ISSN 0907-4449

Structure of the N-terminal domain of human thioredoxin-interacting protein

Galina Polekhina,[a]* David Benjamin Ascher,[b] Shie Foong Kok,[a] Simone Beckham,[a,c] Matthew Wilce[c] and Mark Waltham[b]

[a]Centre for Cancer Research, Monash Institute of Medical Research, Monash University, 27-31 Wright Street, Clayton, VIC 3168, Australia, [b]St Vincent's Institute of Medical Research, 9 Princes Street, Fitzroy, VIC 3065, Australia, and [c]Department of Biochemistry and Molecular Biology, Monash University, Clayton, VIC 3800, Australia

Correspondence e-mail: galina.polekhina@monash.edu

Received 18 September 2012
Accepted 15 November 2012

PDB References: N-terminal domain of TXNIP, 4gei; 4gej

Thioredoxin-interacting protein (TXNIP) is one of the six known α-arrestins and has recently received considerable attention owing to its involvement in redox signalling and metabolism. Various stress stimuli such as high glucose, heat shock, UV, H_2O_2 and mechanical stress among others robustly induce the expression of TXNIP, resulting in the sequestration and inactivation of thioredoxin, which in turn leads to cellular oxidative stress. While TXNIP is the only α-arrestin known to bind thioredoxin, TXNIP and two other α-arrestins, Arrdc4 and Arrdc3, have been implicated in metabolism. Furthermore, owing to its roles in the pathologies of diabetes and cardiovascular disease, TXNIP is considered to be a promising drug target. Based on their amino-acid sequences, TXNIP and the other α-arrestins are remotely related to β-arrestins. Here, the crystal structure of the N-terminal domain of TXNIP is reported. It provides the first structural information on any of the α-arrestins and reveals that although TXNIP adopts a β-arrestin fold as predicted, it is structurally more similar to Vps26 proteins than to β-arrestins, while sharing below 15% pairwise sequence identity with either.

1. Introduction

Thioredoxin-interacting protein (TXNIP), also known as vitamin D_3 up-regulated protein 1 (VDUP-1) or thioredoxin-binding protein 2 (TBP-2), was discovered as a novel binding partner of thioredoxin (TRX) *via* a yeast two-hybrid system (Junn *et al.*, 2000; Nishiyama *et al.*, 1999). The association of TXNIP and TRX results in oxidative stress owing to inhibition of the main redox activity of TRX (Schulze *et al.*, 2004) and affects many cellular pathways regulated by TRX (Powis & Montfort, 2001). TXNIP transcription and protein expression are robustly induced under various stress conditions, including high glucose, UV, H_2O_2, heat shock and mechanical stress, while expression and protein levels of TRX remain unchanged or are down-regulated under several of these conditions (Nishiyama *et al.*, 1999; Schulze *et al.*, 2004). TRX, however, is not the only binding partner of TXNIP, with a number of other protein interactions having recently been identified and being believed to be important in many physiological responses. For instance, TXNIP was shown to activate the inflammasome, a component of the innate immune system, *via* an interaction with the NLRP3 component (Zhou *et al.*, 2010). Several other proteins [JAB1, Fanconi anaemia zinc finger (FAZF), promyelocytic leukaemia zinc finger (PLZF), histone deacetylase 1, pVHL and Dnajb5] have been implicated in

© 2013 International Union of Crystallography
Printed in Singapore – all rights reserved

TXNIP binding (Ago *et al.*, 2008; Han *et al.*, 2003; Jeon *et al.*, 2005; Shin *et al.*, 2008). Thus, TXNIP exerts its cellular functions *via* protein–protein interactions affecting many critical cellular pathways such as redox signalling, glucose and lipid metabolism, the innate immune response, cell proliferation, differentiation, apoptosis, cell-cycle progression and NK cell development (Chung *et al.*, 2006; Kaimul *et al.*, 2007; Kim *et al.*, 2007; Masutani *et al.*, 2012; Patwari & Lee, 2012; Watanabe *et al.*, 2010).

The role of TXNIP in glucose and lipid metabolism was revealed by the observation of a phenotype observed in the mutant mouse strain HcB-19 with a nonsense mutation in the TXNIP gene and was further validated by specific β-cell TXNIP knockouts (Bodnar *et al.*, 2002; Chen, Hui *et al.*, 2008; Chutkow *et al.*, 2008; Hui *et al.*, 2004). Indeed, TXNIP was subsequently shown to inhibit glucose uptake (Patwari *et al.*, 2009). Interestingly, this function of TXNIP appears to be independent of TRX binding. Several gene-array studies on human and rat islets identified TXNIP as the most dramatically glucose-induced genes in insulin resistance/diabetes (Minn *et al.*, 2005; Oka *et al.*, 2009; Qi *et al.*, 2007), and elevated TXNIP levels contribute to the pathologies observed in diabetes (Kobayashi *et al.*, 2003; Qi *et al.*, 2009). The pro-apoptotic properties of TXNIP provide a possible link between glucose toxicity and β-cell death (Chen, Saxena *et al.*, 2008; Shalev, 2008). A lack of TXNIP protects against chemically induced diabetes in mice (Shalev, 2008). Inflammatory mechanisms and mediators of inflammation, which include IL-1β, are believed to contribute to the development and pathogenesis of both forms of diabetes (Cnop *et al.*, 2005; Kristiansen & Mandrup-Poulsen, 2005). Thus, the ability of TXNIP to activate the inflammasome, resulting in processing of IL-1β, further highlights the role of TXNIP in the pathogenesis of diabetes.

The important roles of TRX and the damaging effects of oxidative stress in cardiac function have been known for some time (Berk, 2007; Schulz *et al.*, 2004; Wassmann *et al.*, 2004). Since TXNIP is induced under various stress stimuli, the inhibition of TRX function by TXNIP and the subsequent increase in redox sensitivity is expected to be undesirable in cardiovasculature. Indeed, the specific down-regulation of TXNIP has been shown to be beneficial during heart ischaemia (Xiang *et al.*, 2005).

TXNIP has also been shown to possess tumour-suppressor properties in various cancers, and TXNIP expression is associated with better prognoses (Cadenas *et al.*, 2010; Jeon *et al.*, 2005; Le Jan *et al.*, 2006; Nishinaka *et al.*, 2004; Nishizawa *et al.*, 2011; Piao *et al.*, 2009). Experimental evidence has implicated TXNIP in the metastatic cascade, although the mechanisms and pathways involved have yet to be explored (Cheng *et al.*, 2004; Goldberg *et al.*, 2003). The involvement of TXNIP in glucose homeostasis and its properties as a tumour suppressor may well be intertwined (Peterson & Ayer, 2011).

Based on amino-acid sequences, TXNIP is related to five other genes in the human genome that are now collectively referred to as α-arrestins (Alvarez, 2008). None of the other five α-arrestins bind TRX, but Arrdc4, like TXNIP, has been shown to regulate glucose uptake (Patwari *et al.*, 2009) and Arrdc3 has been implicated in gender-specific obesity (Patwari *et al.*, 2011). TXNIP and the other α-arrestins share a low but undisputed sequence similarity to the better characterized family of β-arrestins and are therefore expected to share structural similarity and functional properties with them (Alvarez, 2008; Aubry *et al.*, 2009). The β-arrestins are involved in G-protein-coupled receptor (GPCR) signalling, receptor internalization and intracellular trafficking (Gurevich *et al.*, 2008; Lefkowitz & Shenoy, 2005). There are only four known β-arrestins, of which two are specific to the eye (visual and cone β-arrestins) and the remaining two account for interactions with all other known GPCRs. It has been suggested that α-arrestins, as more ancient members of the arrestin clan, may also be involved in receptor signalling and endocytosis, thus extending the repertoire of arrestins available for GPCR signalling (Patwari & Lee, 2012).

Structurally, β-arrestins have been well characterized (Gurevich & Gurevich, 2006). They are composed of two structurally similar domains with a curved β-sandwich fold that are related by an approximate twofold symmetry passing through the middle of the molecule. The most distinct structural feature of β-arrestins is the polar core at the junction of the two domains stabilized by the extended C-terminal tail (Hirsch *et al.*, 1999). Upon interaction with the activated and phosphorylated GPCR, the polar core is destabilized by the phosphates, releasing the C-terminal tail to interact with clathryn and AP-2, which engage the GPCR with the endocytosis machinery (Gurevich & Gurevich, 2006).

The crystal structure of Vps26, a component of the retromer complex involved in intracellular trafficking, unexpectedly revealed that Vps26 proteins possess a β-arrestin fold, despite having very low (~10%) sequence identity to β-arrestins (Shi *et al.*, 2006). Based on the sequence alone, the structural relationship between β-arrestins and Vps26 proteins had not been anticipated. Similar to β-arrestins, Vps26 proteins possess a polar core at the junction of the two domains, but in contrast to β-arrestins it is not stabilized by the C-terminal tail and the residues that contribute to the core are not conserved and originate from different structural elements (Collins *et al.*, 2008; Shi *et al.*, 2006).

TXNIP shares a similar twilight (10–15%) pairwise sequence identity with β-arrestins and Vps26 proteins. While the N- and C-terminal domains of β-arrestins as well as Vps26 proteins are structurally related, it is only marginally reflected in their sequence identities of 19% and 17%, respectively. The same is true for TXNIP, with a sequence identity between the N- and C-terminal domains of 15%. Interestingly, another protein, DSCR3, from the Down syndrome critical region shares kinship with both arrestins and Vps26s and has been suggested to represent an intermediate link between the two families (Aubry *et al.*, 2009).

Here, we report the crystal structure of the N-terminal domain of human TXNIP, which provides structural information for an α-arrestin for the first time. TXNIP adopts a β-arrestin fold, as had previously been predicted, but is structurally more similar to Vps26 proteins than to β-arrestins,

Table 1
Data-collection and phasing statistics.

	TXNIP^{149} K64A, native	TXNIP^{149} K64A, K_2PtCl_4	TXNIP^{149}, native
Data collection			
Source	MX2, Australian Synchrotron	MX1, Australian Synchrotron	MX1, Australian Synchrotron
Wavelength (Å)	0.9537	1.0555	0.9537
Space group	*C*2	*C*2	$P2_1$
Unit-cell parameters (Å, °)	*a* = 98.25, *b* = 76.28, *c* = 31.03, β = 92.65	*a* = 97.83, *b* = 76.42, *c* = 31.05, β = 91.64	*a* = 79.74, *b* = 178.81, *c* = 81.89, β = 113.32
Resolution range (Å)	38–1.5 (1.58–1.50)	49–2.61 (2.75–2.61)	46–2.9 (3.06–2.90)
Average mosaicity (°)	0.5	0.64	0.43
Observed reflections	265583 (37090)	102222 (13412)	334580 (46195)
Unique reflections	36857 (5314)	6971 (983)	46358 (6708)
Wilson *B* (Å^2)	19.3	71.5	97.0
Completeness (%)	99.8 (99.2)	98.4 (94.9)†	99.5 (98.8)
Multiplicity	7.2 (7.0)	7.5 (7.0)†	7.2 (6.9)
Mean $I/\sigma(I)$	16.7 (2.6)	34.7 (8.3)	18.5 (2.9)
R_{meas}‡	0.067 (0.727)	0.056 (0.336)†	0.081 (0.719)
$CC_{1/2}$§	0.883 (0.957, 0.426, 0.954)	0.999 (0.765)¶	0.769 (0.614, 0.935, 0.586)
No. of Pt sites		6	
⟨FOM⟩		0.361	
Overall score (BAYES-CC × 100)		49.72 ± 9.15	
Density modification			
R factor		0.2594	
Map skew		0.17	
Correlation of local r.m.s. density		0.86	

† Anomalous pairs were treated separately for merging statistics. ‡ $R_{meas} = \sum_{hkl}\{N(hkl)/[N(hkl)-1]\}^{1/2}\sum_i |I_i(hkl) - \langle I(hkl)\rangle|/\sum_{hkl}\sum_i I_i(hkl)$. § $CC_{1/2}$ is calculated by splitting the data randomly in half. The $CC_{1/2}$ values shown are for the highest resolution shell. The $CC_{1/2}$ values along the principal axes within a maximum angle of 20° are given in parentheses. ¶ The value in parentheses is the $CC_{1/2}$ for anomalous differences over the whole resolution range.

while sharing twilight sequence identity with both. We also demonstrate the formation of a stable TXNIP–TRX complex using purified recombinant proteins that does not appear to involve an intermolecular disulfide bond.

2. Materials and methods

2.1. Protein expression, purification and crystallization

We have previously reported the expression, purification and crystallization of the N-terminal domain of human TXNIP (Polekhina *et al.*, 2011). Briefly, TXNIP^{149} as well as other TXNIP truncations were cloned into a modified pMCSG7 vector in which human TRX^{C73S} was inserted into a *Kpn*I site between the hexahistidine tag (His tag) and the TEV protease recognition site to serve as a solubility tag. Cysteine residues 36, 49 and 120 in TXNIP^{149} and 36, 49, 120, 170, 190, 205, 267 and 333 in TXNIP^{361} were mutated to serines to avoid potential aggregation problems. Two cysteine residues, Cys63 and Cys247, are important for TRX binding and were preserved. The TXNIP^{149} crystals reported by us previously belonged to space group $P2_1$, diffracted to approximately 3 Å resolution and may contain up to 12 molecules in the asymmetric unit. No plausible molecular-replacement solution was obtained using any of the available models of β-arrestins or Vps26 proteins, nor with any of the modifications or combinations that were tested. This was not surprising given the very low (10–15%) pairwise sequence identity between TXNIP and either the β-arrestins or Vps26. SeMet-substituted TXNIP^{149} was produced using a typical minimal medium protocol (Van Duyne *et al.*, 1993) and SeMet incorporation was verified by mass spectrometry and was found to be close to 100%. SeMet-TXNIP^{149} crystallized in conditions similar to those determined for TXNIP^{149}, with the exception that PEG 3350 was used as a precipitant instead of PEG monomethyl ether 5000. However, the SeMet-TXNIP^{149} crystals belonged to space group $C222_1$, with unit-cell parameters *a* = 90.15, *b* = 120.1, *c* = 72.17 Å. Although unexpected, this result was not surprising given that all four methionine residues in TXNIP^{149} are predicted to occur near the surface, thus possibly altering the intermolecular crystal contacts in the SeMet-TXNIP^{149} crystals and resulting in a different crystal form. The calculated Matthews coefficient (V_M) of 2.9 Å^3 Da^{-1} indicates that there are most likely to be two molecules per asymmetric unit, corresponding to a solvent content of 55%. While having fewer molecules per asymmetric unit is beneficial, this crystal form did not lead to a successful structure determination by either anomalous scattering or molecular replacement owing to the small size of the SeMet-TXNIP^{149} crystals and to weak diffraction that extended to only 4–5 Å resolution. We then applied the principle of surface-entropy reduction pioneered by Derewenda in the quest for a more suitable crystal form (Derewenda, 2004). While we followed the rationale proposed by Derewenda to mutate long flexible side chains predicted to be on the surface, such as lysine, arginine or glutamate, to alanine, we took into account the fact that SeMet-TXNIP^{149} had already produced a different crystal form. We therefore decided to mutate the residues expected to be located in the vicinity of the methionines. We mutated Lys64 and Arg93 to alanines. Indeed, TXNIP^{149} K64A promptly produced crystals, also grown in PEG but in a different crystal form, namely space group $P3_121$ (or $P3_221$), with unit-cell parameters *a* = *b* = 104.54, *c* = 134.41 Å. The V_M coefficient of 3.1 Å^3 Da^{-1} suggested the presence of four molecules per asymmetric unit

Table 2
Refinement statistics.

	TXNIP^{149} K64A	TXNIP^{149}
Space group	*C*2	$P2_1$
Resolution (Å)	38.0–1.5	46–2.9
No. of reflections (work/test)	32902/3619	44007/2320
Protein atoms (No. of residues)	1319 (144)	10938 (1366)
No. of solvent molecules	219	0
Ions	0	5
$R/R_{\rm free}$ (%)	17.96/20.33	22.06/29.36
R.m.s. deviations from standard values		
Bond lengths (Å)	0.0147	0.013
Bond angles (°)	1.82	1.82
B factors (Å^2)		
Protein atoms	23.93	89.105
Solvent	36.88	—
Ramachandran plot		
Most favoured regions (%)	93.5	85.7
Disallowed regions (%)	0	0.5

with a solvent content of 60%. The SeMet-TXNIP^{149} K64A crystals grew in the same trigonal space group. As these crystals were thin plates, they diffracted poorly, with diffraction extending only to approximately 6 Å, and were not useful for structure determination. In contrast to TXNIP^{149}, however, TXNIP^{149} K64A could be concentrated to up to 20 mg ml^{-1}, while TXNIP^{149} started to precipitate at around 5 mg ml^{-1}. Over a period of two to four weeks, a 20 mg ml^{-1} solution of TXNIP^{149} K64A in 25 m*M* HEPES pH 7.5, 1 m*M* DTT stored at 277 K produced crystals. We were able to repeat this crystallization process, suggesting that it was not just a chance event. This new crystal form belonged to space group *C*2, with unit-cell parameters a = 98.25, b = 76.28, c = 31.03 Å, β = 92.65°. The crystals diffracted to significantly better than 2 Å resolution and were most likely to contain one molecule per asymmetric unit, with a $V_{\rm M}$ coefficient of 3.4 Å^3 Da^{-1} and a solvent content of approximately 65%.

2.2. Data collection and structure determination

X-ray diffraction data were collected at the Australian Synchrotron (McPhillips *et al.*, 2002). In order to flash-cool the crystals grown from the concentrated protein solution for data collection, they were transferred into a solution with half the protein concentration and 50%(*v*/*v*) glycerol for few minutes prior to flash-cooling. However, in order to perform the heavy-atom soaks, the crystals needed to be transferred to protein-free solution, in which they could be preserved for a period of time without loss of diffraction quality. We chose to use PEG, as all of the other crystal forms of TXNIP had been grown using PEG as a precipitant. Thus, the crystals grown from the concentrated protein solution were transferred for a few minutes into 100 m*M* HEPES pH 7.5, 15% PEG monomethyl ether 5000 and the glycerol concentration was then gradually increased to 15% in 5% steps before flash-cooling. For the Pt soak, the crystals were incubated in 100 m*M* HEPES pH 7.5, 15% PEG monomethyl ether 5000 and 1 m*M* K_2PtCl_4 for 2.5 h prior to flash-cooling as described above.

A 1.5 Å resolution TXNIP^{149} K64A native data set was collected from a single crystal at 100 K on an ADSC Quantum 315r detector at the MX2 station. A total rotation of 360° was recorded with 1° rotation and an exposure time of 2 s per frame. A data set from a single Pt-soaked TXNIP^{149} K64A crystal was collected at 100 K on an ADSC Quantum 210r detector at the MX1 station. A total rotation of 720° was performed using inverse-beam geometry with a wedge of 45°, 1° rotation and an exposure time of 1 s per frame. A 360° rotation data set was recorded from a single TXNIP^{149} crystal at 100 K on an ADSC Quantum 210r detector at the MX1 station with 1° rotation and an exposure time of 2 s per frame. All diffraction data were processed using *MOSFLM* (Leslie, 1992) and scaled using *SCALA* from the *CCP*4 suite (Winn *et al.*, 2011). X-ray data-processing statistics are shown in Table 1.

The structure of TXNIP^{149} K64A in the *C*2 crystal form was determined by single anomalous dispersion using the Pt diffraction data. *phenix.autosol* generated a polyalanine model comprising 112 of 150 residues (Adams *et al.*, 2010). Details of the phasing and density-modification statistics are shown in Table 1. *phenix.autobuild* subsequently built most of the model, with the exception of the flexible N-terminus (residues 0–5) and residues 80–86 of the flexible solvent-exposed loop. Judging by the coordinates of the heavy atoms determined by *phenix.autosol*, the sulfur groups of Met57 and Met88 served as ligands for a Pt chloride compound. The model of TXNIP^{149} K64A was refined against the 1.5 Å resolution native data set using *REFMAC*5 (Murshudov *et al.*, 2011). Residues in loop 80–86 were manually built in the later refinement stages. *Coot* was used throughout for model rebuilding (Emsley *et al.*, 2010). The final model of TXNIP^{149} K64A comprises residues 6–149 of TXNIP and was refined to 1.5 Å resolution with an *R* factor of 17.96% and an $R_{\rm free}$ of 20.33%. Refinement statistics are shown in Table 2. The model is of excellent quality, with 93.5% of the residues in the most favoured regions and no residues in the disallowed regions of the Ramachandran plot. Residues 80–86 form a solvent-exposed flexible loop that was built into weak electron density with two different conformations. Residues 114–120 are flexible, but have a very well defined electron density and were modelled as having two very similar conformations.

The structure of TXNIP^{149} in the $P2_1$ crystal form was determined by molecular replacement using the structure of TXNIP^{149} K64A as a search model. The $P2_1$ crystal form contained ten molecules per asymmetric unit. The program *MOLREP* (Vagin & Teplyakov, 2010) was able to position five molecules. Upon inspection of the electron-density map, it was found that residues 52–67 of the long β-hairpin adopted a slightly different conformation to that of the search model and they were rebuilt. Following a cycle of refinement, it became clear, based on the electron density, that for each of the five molecules located by molecular replacement there is an additional molecule related by twofold noncrystallographic symmetry. Residues 62–64 of each molecule participate in the main-chain hydrogen-bonding pattern characteristic of the antiparallel β-sheet in each of the five pairs of molecules. The final solution is in agreement with the self-rotation function, showing several twofold axes perpendicular to the crystallographic 2_1 axis and a fourfold axis parallel to the

crystallographic 2_1 axis (Polekhina *et al.*, 2011). The TXNIP^{149} structure in the $P2_1$ crystal form was refined using *REFMAC*5 to 2.9 Å resolution with an R factor of 22.1% and an R_{free} of 29.4%. Jelly-body refinement was used in the early refinement stages. TLS parameterization for each chain and noncrystallographic symmetry restraints applied to the core of the molecule were employed throughout the refinement. The isotropic B factors were also refined in the final stages. The model is of adequate quality, given the moderate resolution of the diffraction data. Owing to disorder, loops 80–86 and 112–120 could not be modelled in several molecules. 85.7% of the residues were in the most favoured regions of the Ramachandran plot, with only 0.5% of the residues (corresponding to areas adjacent to the flexible loops) falling in the disallowed regions of the plot. Refinement statistics are shown in Table 2. Structure factors and coordinates have been deposited in the Protein Data Bank with codes 4gei for the 1.5 Å resolution TXNIP^{149} K64A structure and 4gej for the 2.9 Å resolution TXNIP^{149} structure.

2.3. TXNIP–TRX complex formation and its analysis by multi-angle light scattering and mass spectrometry

The expression and purification of TXNIP^{361} followed a procedure similar to that described above for TXNIP^{149}, except that following TEV cleavage TXNIP^{361} was separated from the His-tagged TRX^{C73S} by elution in the flowthrough fraction in loading buffer (20 m*M* sodium phosphate pH 7.4, 500 m*M* NaCl, 20 m*M* imidazole) plus 10 m*M* DTT. Human TRX^{C73S} was cloned into pMCSG7 vector and purified on a HisTrap column (GE Healthcare). The His tag was cleaved using TEV protease. The human TRX^{C73S} was separated from the His tag and His-tagged TEV using a HisTrap column. The purified TRX^{C73S} was dialysed against 20 m*M* sodium phosphate pH 7.4, 150 m*M* NaCl, 5 m*M* DTT. For complex formation, TXNIP^{361} and TRX^{C73S} were mixed in a 1:2 ratio, dialysed overnight against a buffer consisting of 20 m*M* sodium phosphate pH 7.4, 150 m*M* NaCl, 0.1 m*M* DTT and concentrated prior to size-exclusion chromatography. The formation of the complex was monitored using size-exclusion chromatography-coupled multi-angle light scattering (SEC-MALS) on a Superdex 200 10/300 GL column (GE Healthcare) in the same buffer as used for dialysis. MALS was used to estimate the molecular weight. The chromatographic system comprised a Shimadzu DGU-20A5 degasser, an LC-20AD liquid chromatograph, an SIL-20AHT auto-sampler, a CBM-20A communications bus module, an SPD-20A UV–Vis detector and a CTO-20AC column oven coupled to a Wyatt Technology DAWN HELEOS-II light-scattering detector fitted with an Optilab T-rEX refractive-index detector. System calibration was performed against bovine serum albumin (Sigma–Aldrich). Data collection and analysis were performed using the *ASTRA* v.6.0 software (Wyatt Technology). The TXNIP^{361}–TRX^{C73S} complex was also analysed by mass spectrometry using an Agilent Q-TOF LC/MS with a C8 column and a gradient of 5–75% acetonitrile in 0.1% formic acid.

3. Results and discussion

3.1. Overall structure

The structure of the N-terminal domain of human TXNIP was determined by X-ray crystallography using the single anomalous dispersion technique with Pt-soaked native crystals. The high-resolution structure of TXNIP^{149} K64A in the $C2$ crystal form was refined to 1.5 Å resolution. The final model included residues 6–149 of human TXNIP. We have also refined the structure of TXNIP^{149} in the $P2_1$ crystal form to 2.9 Å resolution. The N-terminal domain of TXNIP adopts a β-sandwich fold made up of two antiparallel β-sheets composed of three and four β-strands, respectively (Fig. 1). Two short antiparallel β-strands located in the $\beta2$–$\beta3$ and $\beta4$–$\beta5$ connections cap one side of the β-sandwich domain. Two additional short parallel β-strands, one in the $\beta1$–$\beta2$ connection and another following $\beta7$ at the end of the N-terminal domain, cap the other side of the molecule. There is a classic β-bulge involving residues Glu68-Tyr69-Leu70 in $\beta4$.

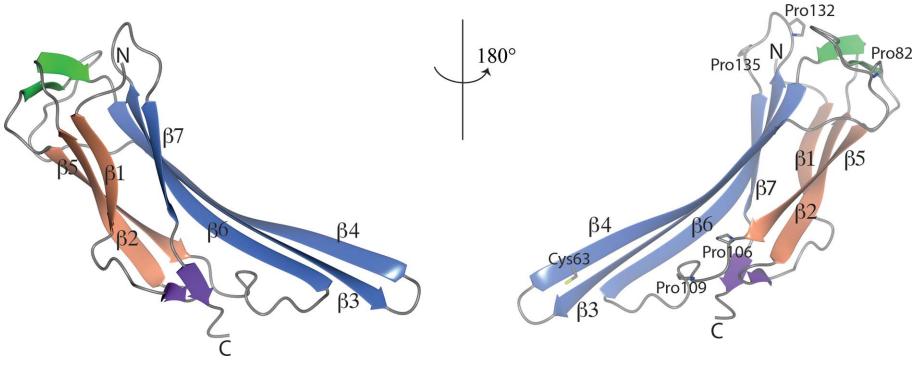

Figure 1
Overall structure of the N-terminal domain of human TXNIP: two views 180° apart are shown as ribbons. The two antiparallel β-sheets forming a β-sandwich are shown in different colours: the convex side in orange and the concave side in blue. Cys63, which is essential for effective TRX binding, as well as the proposed SH3-binding sites, are shown as sticks. All structural figures were prepared with *CCP4mg* (McNicholas *et al.*, 2011).

In the $C2$ crystal form, a single molecule of TXNIP^{149} K64A in the asymmetric unit forms extensive interactions with two symmetry-related molecules, forming a continuous antiparallel β-sheet *via* a main-chain hydrogen-bond network involving residues 66–68 of the two symmetry-related molecules on one side and residues 117–121 on the other side (Fig. 2*a*). These interactions are supplemented by a number of hydrogen bonds between the side chains and a combination of side-chain and main-chain interactions at either end of the antiparallel β-sheet, including Gln61 NE2 to the main-chain carbonyl of Glu104, Gln61 OE2 to the main-chain amide of Glu104, Lys117

NZ to Glu144 OE2, Gln58 NE2 to Glu104 OE1 and the main-chain carbonyl of Tyr69 to Gln65 NE2. There are also interactions between the two symmetry-related molecules on each side: the main-chain carbonyl of Lys8 to the main-chain amide of Glu85, Lys8 NZ to Glu87 OE1, and the main-chain carbonyl of Thr83.

In the $P2_1$ crystal form, ten molecules of TXNIP^{149} in the asymmetric unit are arranged in pairs stacked on top of each other and related by pseudo-4_1 symmetry. The packing is consistent with the self-rotation function (Polekhina *et al.*, 2011). The two TXNIP^{149} molecules in each pair are related by twofold symmetry *via* the main-chain hydrogen-bonding network characteristic of the antiparallel β-sheet, involving residues 62–64 from each monomer. In addition, there is a hydrogen bond between Ser61 OG and Asn66 NE2 and a disulfide bond between Cys63 from each monomer (Fig. 2*b*). This disulfide bond is apparent in the electron density in each of the five pairs of TXNIP^{149} molecules in the asymmetric unit, despite the presence of 1–2 m*M* DTT in the protein solution prior to crystallization. The main difference between the molecules of TXNIP^{149} in the $P2_1$ crystal form and those in the *C*2 crystal form concerns the conformation of the β-hairpin formed between the end of β3 and the beginning of β4 (Fig. 2*c*). The loop connecting β5 and β6 located next to the β3–β4 hairpin (residues 112–120) also adopts slightly different conformations. The flexibility of these regions is not surprising given that the equivalent regions in β-arrestins and Vps26s adopt considerably different conformations. Our crystallization constructs also did not include the C-terminal domain of TXNIP, which is expected to be in contact with these loops. The long solvent-exposed loop (comprising residues 80–86) that connects β4 and the following short β-strand also appears to be flexible.

3.2. Surface electrostatic potential of the TXNIP N-terminal domain

As TXNIP is expected to participate in multiple protein–protein interactions in order to exert its biological activities, we looked for the presence of specific features affecting the surface electrostatic potential of the N-terminal domain of TXNIP (Fig. 3). In β-arrestins, both sides of the β-sandwich domains at the N- and C-termini are known to be involved in protein–protein interactions. The concave surface of the

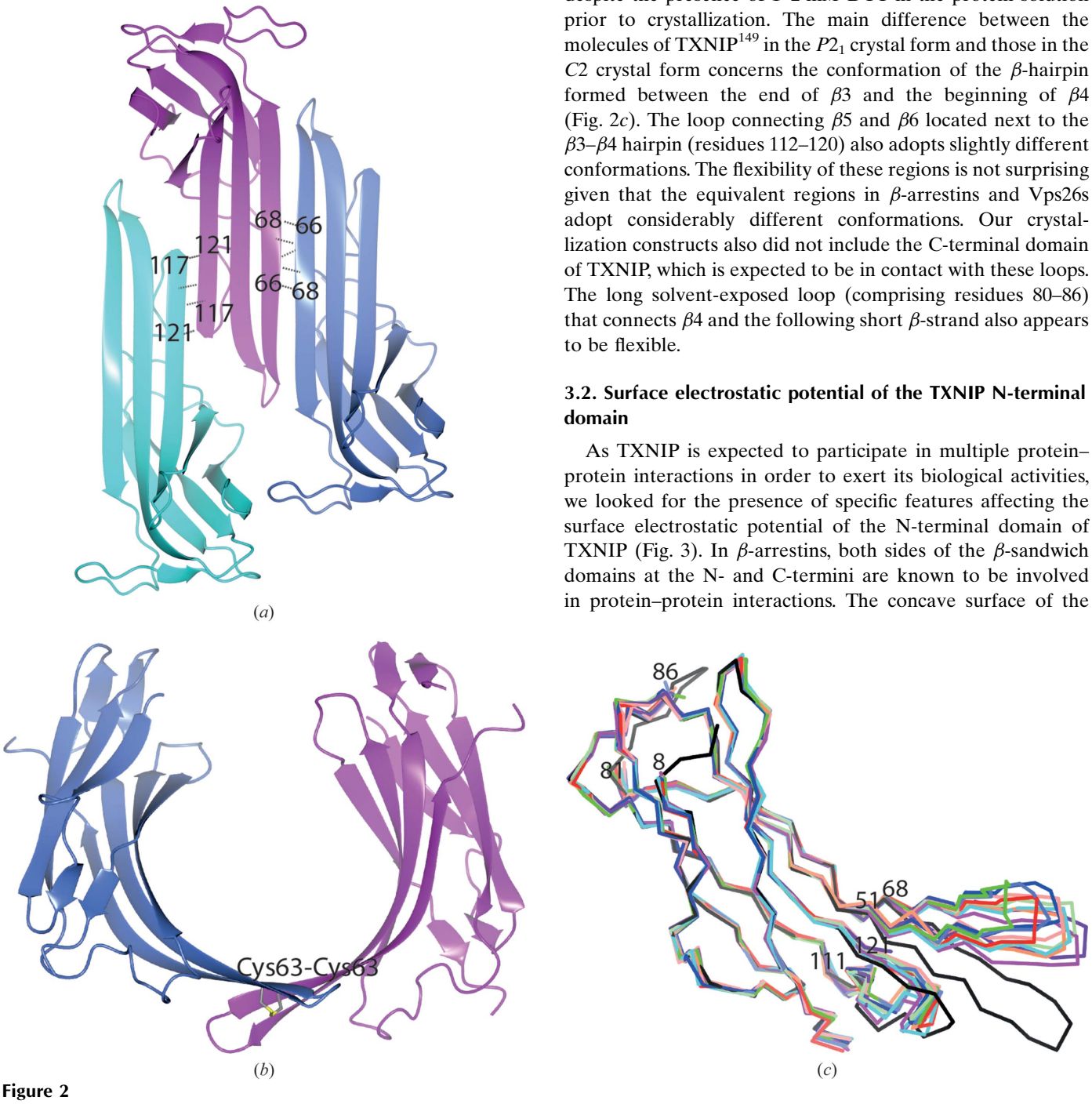

Figure 2
Structure of the N-terminal domain of TXNIP in different crystal forms. (*a*) The N-terminal domain of TXNIP in the *C*2 crystal form (magenta) and two symmetry-related molecules (cyan and blue). (*b*) The Cys63–Cys63 disulfide-linked dimer of the N-terminal domain of TXNIP observed in the $P2_1$ crystal form. (*c*) The superimposition of the N-terminal domain of TXNIP in the *C*2 crystal form (black) and the ten crystallographically independent molecules in the $P2_1$ crystal form.

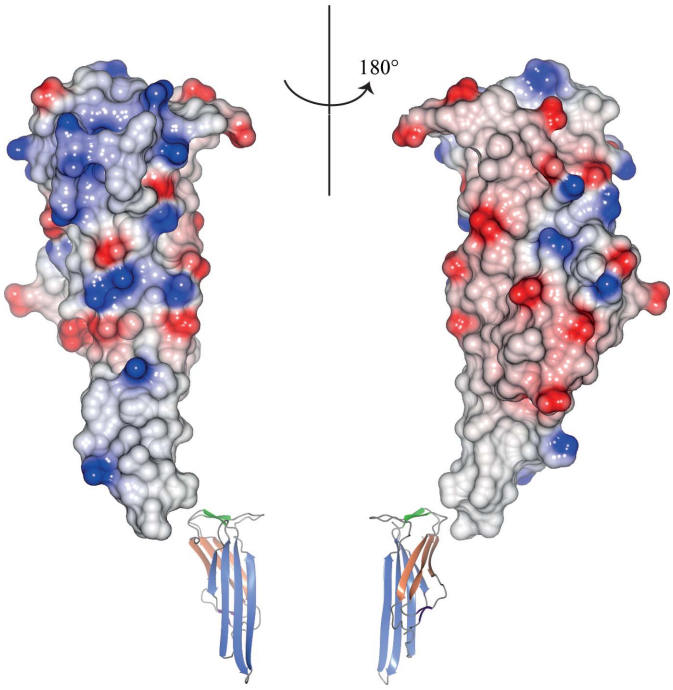

Figure 3
The surface of the N-terminal domain of TXNIP (*C*2 crystal form) coloured by electrostatic potential, with the corresponding orientations of the molecule shown in ribbons below.

N-terminal domain of TXNIP appears to be more positively charged than the convex surface, although there is no particular clustering of charge. The end of the domain expected to face and interact with the C-terminal domain is neutral, suggesting that the inter-domain junction of TXNIP is unlikely to have a buried polar core similar to those that are present in β-arrestins and Vps26 proteins.

3.3. Structural homology of TXNIP to β-arrestins and Vps26 proteins

Based on their low (~10%) sequence identities, TXNIP is expected to be structurally related to β-arrestins. The retromer subunit Vps26 proteins involved in intracellular trafficking are structurally related to β-arrestins and share twilight sequence identity with them. The TXNIP and Vps26 proteins also share very low (less than 15%) sequence identities. Despite low sequence identities with either β-arrestins or Vps26 proteins, the N-terminal domain of TXNIP adopts a β-sandwich fold characteristic of β-arrestins and Vps26 proteins. Indeed, superimposition of TXNIP on Vps26A (PDB entry 2fau; Shi *et al.*, 2006) and Vps26B (PDB entry 2r51; Collins *et al.*, 2008) using 52 C^{α} atoms (of residues 8–15, 24–34, 43–49, 71–75, 97–103, 123–129 and 136–143 of TXNIP on residues 12–19, 45–55, 67–73, 90–94, 105–111, 130–136 and 142–148 of Vps26A and residues 10–17, 43–53, 65–71, 88–92, 103–109, 128–134 and 140–146 of Vps26B) results in r.m.s.d. values of 1.03 and 0.94 Å, respectively, while superimposition of TXNIP on visual arrestin (PDB entry 1cf1), nonvisual arrestin-1 and arrestin-2 (PDB entries 1g4m and 3p2d; Han *et al.*, 2001; Zhan *et al.*, 2011) and cone arrestin (PDB entry 1suj; Sutton *et al.*, 2005) using 60 C^{α} atoms (of residues 10–14, 26–33, 43–51, 68–76, 97–107, 120–129 and 139–146 of TXNIP on residues 22–26, 40–47, 56–64, 82–90, 114–124, 144–153 and 170–177 of visual arrestin, residues 18–22, 36–43, 52–60, 78–86, 111–121, 141–150 and 164–171 of nonvisual arrestin-1, residues 19–23, 37–44, 53–61, 79–87, 112–122, 142–151 and 165–172 of nonvisual arrestin-2 and residues 17–21, 35–42, 51–59, 77–85, 108–118, 138–147 and 161–168 of cone arrestin) gives r.m.s.d. values of 1.28, 1.20, 1.25 and 1.26 Å, respectively. These values are similar to those obtained when β-arrestins are compared with Vps26 proteins. Unexpectedly, however, TXNIP[149] is structurally more similar to Vps26 proteins than to β-arrestins (Fig. 4). The N-terminal β-strand present in β-arrestins that interacts with the C-terminal tail, the α-helix and the second short α-helix are all absent in TXNIP as well as in Vps26 proteins. The distinct long β-hairpin insertion between the first and second β-strands in Vps26 proteins is absent in both β-arrestins and TXNIP[149]. Fig. 5 shows the structure-based sequence alignment of TXNIP[149], Vps26A, Vps26B, visual arrestin, nonvisual arrestin-1 and arrestin-2 and cone arrestin using their N-terminal domains.

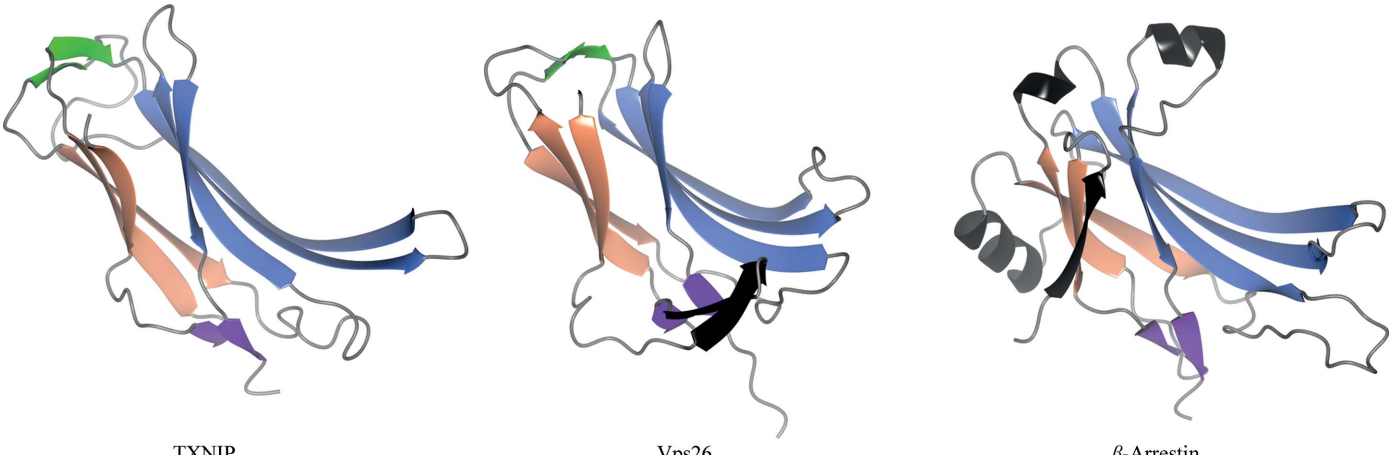

Figure 4
Side-by-side comparison of the N-terminal domains of TXNIP, Vps26 and visual β-arrestin following their structural superimposition. The structural features that are unique to Vps26 and β-arrestins are highlighted in black.

3.4. The proposed SH3-binding sites in the N-terminal domain of TXNIP do not exist

Based on the presumed structural and functional relationships between TXNIP and β-arrestins, TXNIP has been suggested to contain SH3-binding sites at both the Pro106–Pro109 and Pro132–Pro135 motifs (Fig. 1; Spindel *et al.*, 2012). Based on our structure of TXNIP[149], these motifs are unlikely to be capable of interacting with SH3 domains in a typical Pro-rich peptide manner, as such interactions would result in steric clashes. During an investigation of the structural motifs that contribute to metabolic functions, the discovery was made that the TXNIP P135L mutant severely affects the nuclear localization of TXNIP (Patwari *et al.*, 2009). Our structure of TXNIP[149] provides insight into why this may occur. One of the monopartite nuclear-localization sequences in TXNIP (residues 5–8; KKIK) is located spatially close to Pro135. The long flexible solvent-exposed loop, which is unique to TXNIP (residues 80–86, including Pro82; Fig. 1), might be a more likely candidate to participate in protein–protein interaction, even though its sequence does not resemble those of typical SH3-binding motifs.

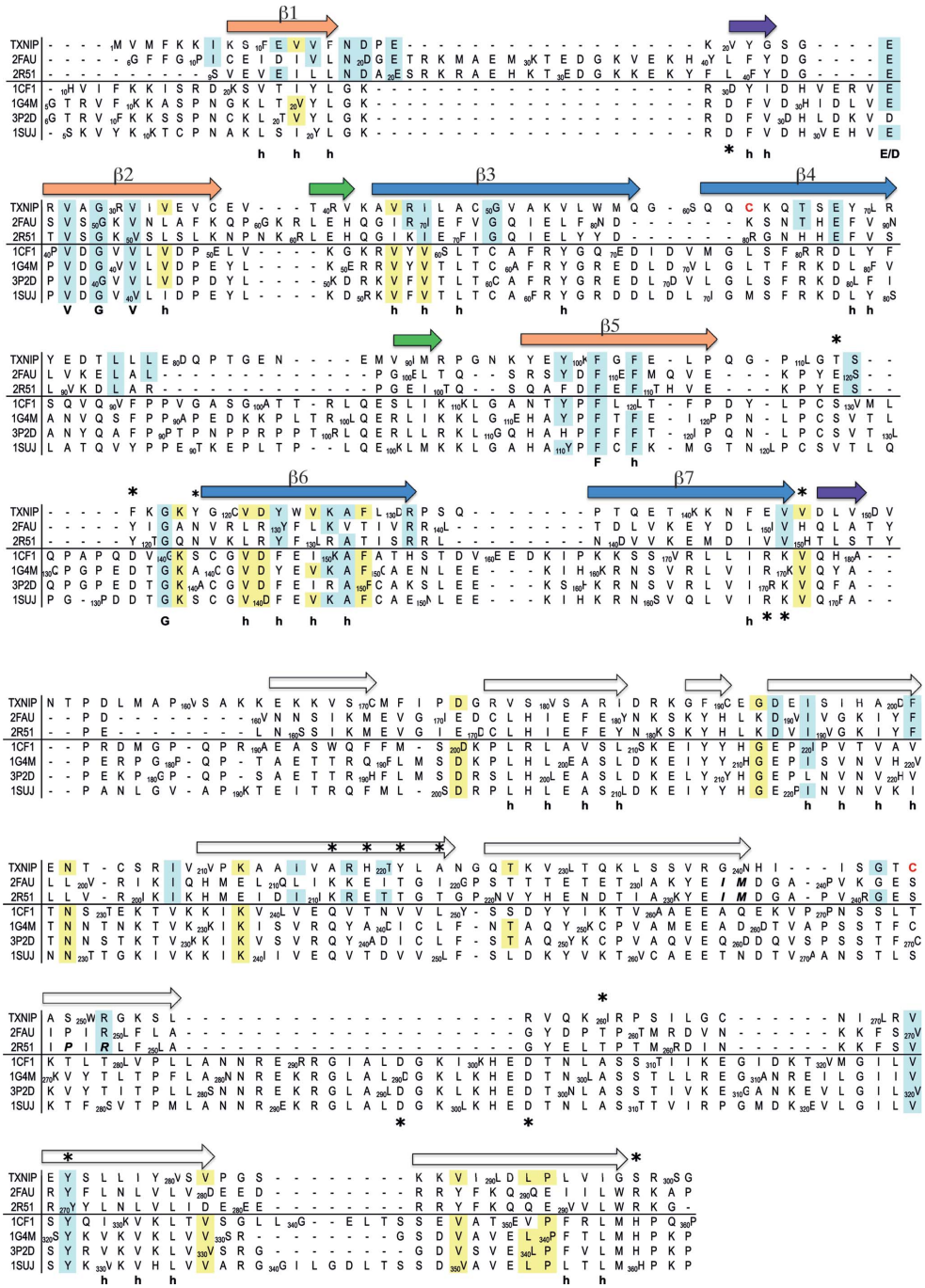

Figure 5
Structure-based sequence alignment of the N-terminal domains of TXNIP, Vps26A (PDB entry 2fau), Vps26B (PDB entry 2r51), visual β-arrestin (PDB entry 1cf1), β-arrestin-1 (PDB entry 1g4m), β-arrestin-2 (PDB entry 3p2d) and cone β-arrestin (PDB entry 1suj) and the sequence alignment of the C-terminal domains of TXNIP, Vps26A and Vps26B, with the structure-based sequence alignment of Vps26A, Vps26B and β-arrestins. The asterisks above the sequences indicate the residues in the polar core of the Vps26 proteins (smaller asterisks indicate involvement of the main-chain atoms rather than the side-chain atoms); the asterisks below the sequences identify the residues contributing to the polar core in the β-arrestins. The two cysteine residues in TXNIP identified as being important for TRX binding are shown in red. The residues in Vps26 proteins implicated in binding to Vps35 are shown in bold italic.

3.5. Model of full-length TXNIP and its implications

Based on our finding that the N-terminal domain of TXNIP is structurally more similar to the Vps26 proteins than to the β-arrestins, we propose that the Vps26 proteins are a better template to model the C-terminal domain of TXNIP than the β-arrestins. We produced a structure-based sequence alignment of the N-terminal domains of TXNIP, Vps26A, Vps26B, visual arrestin, nonvisual β-arrestin-1 and β-arrestin-2 and cone β-arrestin, together with a sequence alignment of the C-terminal domains of TXNIP, Vps26A and Vps26B. A structure-based sequence alignment of Vps26 proteins with β-arrestins over their C-terminal domain was added (Fig. 5). Based on this alignment, a model of the C-terminal domain of TXNIP (residues 164–300) was

constructed with *MODELLER* v.9.10 using the crystal structures of Vps26 proteins as templates (Marti-Renom *et al.*, 2000). The linker between the N- and C-terminal domains in TXNIP is 12 and 5–6 residues longer than the linkers in Vps26 proteins and β-arrestins, respectively. Therefore, instead of modelling the linker, we used *3D-Dock* (Moont *et al.*, 1999) to dock the model of the C-terminal domain to the structures of the N-terminal domain of TXNIP. These included the structure of the N-terminal domain of TXNIP in the *C*2 crystal form and the three crystallographically independent molecules in the $P2_1$ crystal form in which the loops that are expected to face the C-terminal domain were modelled, as these are present in slightly different conformations. The top docking solution for one of the N-terminal domain structures in the $P2_1$ crystal form and the model of the C-terminal domain produced an arrangement of the arrestin domains resembling that found in Vps26 proteins and β-arrestins (Fig. 6). The distance of 36.8 Å between the last C^{α} atom in $TXNIP^{149}$ and the C^{α} atom of the first modelled residue in the C-terminal domain can be comfortably bridged by the 14-residue linker, making this model of the full-length TXNIP molecule plausible.

β-Arrestins possess the buried polar core at the junction of the N- and C-terminal domains involved in the recognition of the phosphorylated residues of the receptor. This polar core is the most distinct structural feature of the β-arrestins. In Fig. 5, the asterisks below the sequences highlight the residues that contribute to the polar core in β-arrestins. Although Vps26 proteins also possess a polar core, a different set of residues highlighted by asterisks above the sequences is involved (Fig. 5). The equivalent residues in TXNIP are not conserved and thus TXNIP is unlikely to possess a polar core similar to that of either Vps26 proteins or β-arrestins. Moreover, the inter-domain junction in TXNIP might be of a more hydrophobic nature. Based on the three-dimensional structure of the N-terminal domain of TXNIP and the structural model of full-length TXNIP, the residues that are likely to contribute to the interface between the N- and C-terminal domains are Val54, Trp56, Tyr118, Cys63, Lys115, Lys117 and Gln58 from the N-terminal domain and Tyr221, His219, Leu230, Leu270, Cys267, Ile269, Lys228 and Asn268 from the C-terminal domain.

Two cysteine residues in TXNIP, Cys63 and Cys247, have been shown to be important for the interaction with TRX (Patwari *et al.*, 2006). While Cys247 is essential for binding to

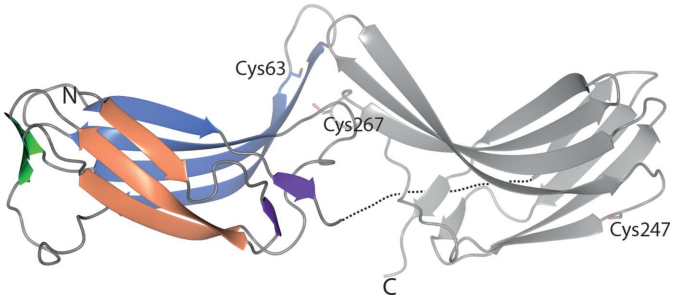

Figure 6
Ribbon representation of the model of full-length TXNIP constructed from the structure of the N-terminal domain of TXNIP (coloured) and the model of the C-terminal domain (grey). The model was built with *MODELLER* v.9.10 using the Vps26A and Vps26B structures as templates, followed by docking. The linker between the N- and C-terminal domains is shown as a black dashed line.

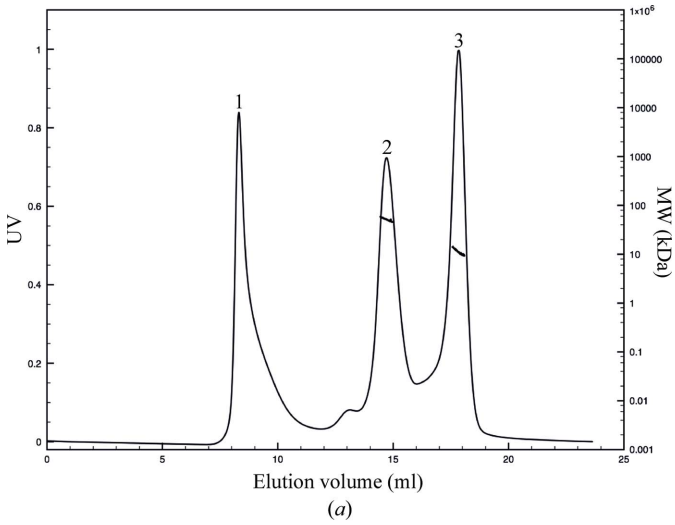

(*a*)

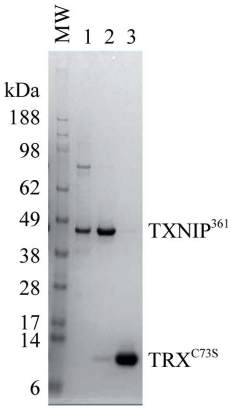

	Peak 2	Peak 3
Elution volume (ml)	14.5–15.0	17.6–18.1
Mn	51 410 (±0.9%)	11 090 (±2.1%)
Mp	51 310 (±0.8%)	10 960 (±1.7%)
Mw	51 630 (±0.9%)	11 240 (±2.1%)
Mz	51 860 (±2.0%)	11 400 (±4.7%)
Polydispersity		
Mw/Mn	1.004 (±1.3%)	1.014 (±3.0%)
Mz/Mw	1.009 (±2.2%)	1.028 (±5.1%)

(*b*)

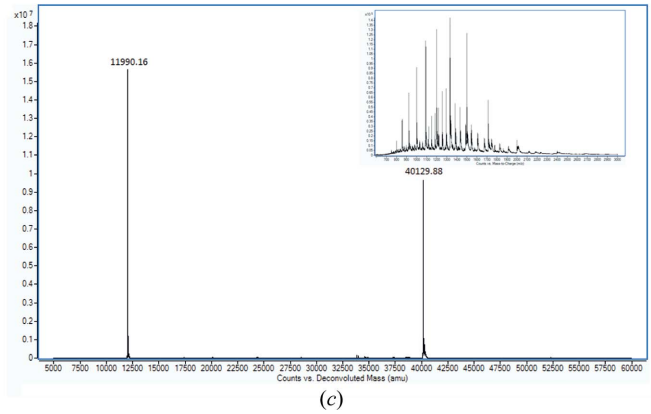

(*c*)

Figure 7
Complex formation between $TXNIP^{361}$ and TRX^{C73S} as observed by Superdex 200 size-exclusion chromatography coupled to MALS. (*a*) The chromatographic UV trace with molecular weight from the MALS data. (*b*) 4–12% SDS–PAGE gel and a table of molecular weights determined from the MALS data. (*c*) Deconvoluted ESI-TOF mass spectrum of the $TXNIP^{361}$–TRX^{C73S} complex (peak 2) eluted from Superdex 200. The raw MS data plotted as intensity *versus* the mass-to-charge ratio are shown in the inset.

TRX, Cys63 is important for effective binding. Cys63 and Cys247 have been suggested to be involved in an intramolecular disulfide bond, which would be reduced upon interaction with TRX, resulting in the formation of a covalent TXNIP–TRX complex *via* an intermolecular disulfide bond between Cys247 of TXNIP and Cys32 of TRX (Patwari *et al.*, 2006). Cys63 is located at the tip of the $\beta3$–$\beta4$ hairpin, in the area of the expected interaction site with the C-terminal domain of TXNIP. As mentioned above, we observed covalently linked dimers of TXNIP^{149} *via* Cys63–Cys63 in the $P2_1$ crystal form, although this is most likely to be a crystallization artefact. In the model of full-length TXNIP, Cys247 is located at least 50 Å away from Cys63 (Fig. 6). The arrangement of the N- and C-terminal domains in TXNIP is expected to be similar to those in β-arrestins and Vps26 proteins. In this case, the intramolecular disulfide bond between Cys63 and Cys247 in TXNIP is unlikely to be formed and the contribution of Cys63 to TRX binding remains unknown. Interestingly, however, the equivalent of residue Cys247 in TXNIP is located in the loop of the Vps26 proteins that has been identified as the binding site for Vps35, another component of the retromer subunit and a binding partner of Vps26 in the retromer complex. Cys267, which is conserved among α-arrestins, is located in the model of the full-length TXNIP such that it is in the vicinity of Cys63 and is possibly able to form an intramolecular disulfide bond with Cys63, although neither Cys63 nor Cys247 are conserved among α-arrestins and none of the other α-arrestins bind TRX.

3.6. Interaction of TXNIP and TRX

We have identified a successful expression system for the production of TXNIP for structural and functional studies (Polekhina *et al.*, 2011). The expression construct codes for His-tagged human TRX^{C73S}, a TEV protease recognition site and various TXNIP truncations. The use of human TRX as a solubility tag is essential for the expression of soluble TXNIP. Even though bacterial TRX is sometimes used as a solubility tag, it was not effective in the expression of soluble TXNIP. Thus, the use of the binding partner as a protein solubility tag in this case has been successful, and this strategy may be useful in other cases involving binary complexes. In addition, following the TEV cleavage of the fusion protein the two binding partners TRX and TXNIP are present in an equimolar ratio and complex formation can be observed using size-exclusion chromatography.

We reported previously that TXNIP^{149} does not bind TRX (Polekhina *et al.*, 2011), whereas TXNIP^{361} binds as described above. Following TEV cleavage, a small fraction of the fusion protein always remained uncleaved and eluted together with the complex. We therefore attempted to isolate TXNIP^{361} from His-tagged TRX and the uncleaved fusion using a HisTrap column following TEV cleavage. The concentration of DTT needed to be raised to 10 m*M* in order for TXNIP to elute in the flowthough fraction and at the same time to allow the His-tagged TRX and the uncleaved fusion protein to be retained on the column. We have purified human TRX^{C73S} from which the His tag has been removed. For the formation of the TXNIP^{361}–TRX^{C73S} complex, TXNIP^{361} and TRX^{C73S} in a 1:2 molar ratio were dialysed against 20 m*M* sodium phosphate, 150 m*M* sodium chloride, 0.1 m*M* DTT pH 7.4, concentrated and purified by Superdex 200 10/300 GL size-exclusion chromatography coupled to MALS. Prior to complex formation, TXNIP^{361} was eluted in buffer containing 10 m*M* DTT. Therefore, it seems unlikely that Cys63 and Cys247 would form an intramolecular disulfide bond, which is in agreement with the structural modelling described above. It is critical that TRX is fully reduced by dialysis in buffer containing at least 5 m*M* DTT prior to complex formation, as the oxidized TRX does not interact with TXNIP. We observed the formation of a stable monodisperse complex between TXNIP^{361} and TRX^{C73S} in a 1:1 ratio (Figs. 7*a* and 7*b*). There did not appear to be an intermolecular disulfide bond between TXNIP^{361} and TRX^{C73S}, as the complex appeared as two bands corresponding to the expected molecular weights of TXNIP^{361} and TRX^{C73S} in either reducing or nonreducing SDS–PAGE conditions. In addition, analysis of the TXNIP^{361}–TRX^{C73S} complex by mass spectrometry did not detect a covalent intermolecular complex *via* a proposed mixed disulfide bond between Cys247 of TXNIP and Cys32 of TRX (Fig. 7*c*).

We observed a fraction of TXNIP^{361} alone as an aggregate that did not interact with TRX^{C73S}. A fraction of TRX^{C73S} alone was also observed, as an excess of TRX^{C73S} was used for formation of the complex (Figs. 7*a* and 7*b*). The propensity of TXNIP to form aggregates may have functional significance, as β-arrestins are known to form aggregates. The ability of visual β-arrestin to oligomerize at high concentrations allows a large reserve of inactive multimeric visual β-arrestin to be maintained until it is required for the rapid desensitization of the cognate receptor rhodopsin (Hirsch *et al.*, 1999; Schubert *et al.*, 1999). The oligomerization of nonvisual β-arrestin, which is promoted by inositol hexakisphosphate binding, has been shown to negatively regulate the interaction of nonvisual β-arrestin with the plasma membrane and nuclear signalling proteins (Milano *et al.*, 2006). It is possible that TXNIP, which is rapidly induced under various conditions, also utilizes oligomerization for purposes such as storage or to vary its downstream effects, depending on the conditions.

4. Conclusions

The crystal structure of the N-terminal domain of human TXNIP provides the first structural information on any of the six α-arrestins, which together form an evolutionarily more ancient protein family than the remotely related β-arrestin family. The three-dimensional structure reveals that although TXNIP adopts the predicted typical β-arrestin fold, it is structurally more similar to Vps26 proteins than to β-arrestins, while sharing a similar twilight (10–15%) level of sequence identity to both. The structure of the N-terminal domain of TXNIP shows that the proposed P^{106}QGP^{109} and P^{132}SQP^{135} SH3-binding motifs are unlikely to be able to interact with SH3 domains in a typical manner. The structure offers a

plausible explanation as to why the P135L mutation impacts on the nuclear localization of TXNIP. Cys63 in the N-terminal domain of TXNIP (shown to be essential for effective binding to TRX) is located in a β-hairpin, where it is expected to face the C-terminal domain of TXNIP. This residue has been suggested to form an intramolecular disulfide bond with Cys247 of the C-terminal domain of TXNIP which is reduced upon interaction with TRX. Based on the generated full-length model of TXNIP, Cys247 is expected to be located as far as 50 Å away from Cys63. Therefore, the existence of an intramolecular disulfide bond between Cys63 and Cys247 in TXNIP seems unlikely. In addition, a stable and monodisperse complex between $TXNIP^{361}$ and TRX^{C73S} was observed by size-exclusion chromatography coupled to MALS at a 1:1 stoichiometry; this complex does not appear to involve a mixed disulfide bond between Cys247 of TXNIP and Cys32 of TRX.

GP was the recipient of a Career Development Award (502724) from the National Health and Medical Research Council (NHMRC) of Australia. This work was supported by a grant (448305) from NHMRC to GP and Mark Waltham. Matthew Wilce is an NHMRC Senior Research Fellow and SB is supported by an NHMRC grant. We acknowledge the funding for MALS equipment from the Australian Research Council and the Victorian Government's Operational Infrastructure Support Program. DBA was an Australian Postgraduate Award Scholar as well as a recipient of a St Vincent's Institute Foundation Scholarship sponsored by Colin North and Major Engineering. This research was undertaken at the Australian Synchrotron, Victoria, Australia. We appreciate the support provided by all staff at the Australian Synchrotron during our visits. We would also like to acknowledge the staff, and particularly Dr Janet Newman, at the Bio21 Collaborative Crystallographic Centre at CSIRO Molecular and Health Technologies, Parkville, Melbourne. We thank Frances Cribbin for help with the manuscript.

References

Adams, P. D. *et al.* (2010). *Acta Cryst.* D**66**, 213–221.

Ago, T., Liu, T., Zhai, P., Chen, W., Li, H., Molkentin, J. D., Vatner, S. F. & Sadoshima, J. (2008). *Cell*, **133**, 978–993.

Alvarez, C. E. (2008). *BMC Evol. Biol.* **8**, 222.

Aubry, L., Guetta, D. & Klein, G. (2009). *Curr. Genomics*, **10**, 133–142.

Berk, B. C. (2007). *Trans. Am. Clin. Climatol. Assoc.* **118**, 209–214.

Bodnar, J. S. *et al.* (2002). *Nature Genet.* **30**, 110–116.

Cadenas, C. *et al.* (2010). *Breast Cancer Res.* **12**, R44.

Chen, J., Hui, S. T., Couto, F. M., Mungrue, I. N., Davis, D. B., Attie, A. D., Lusis, A. J., Davis, R. A. & Shalev, A. (2008). *FASEB J.* **22**, 3581–3594.

Chen, J., Saxena, G., Mungrue, I. N., Lusis, A. J. & Shalev, A. (2008). *Diabetes*, **57**, 938–944.

Cheng, G. C., Schulze, P. C., Lee, R. T., Sylvan, J., Zetter, B. R. & Huang, H. (2004). *Exp. Cell Res.* **300**, 297–307.

Chung, J. W., Jeon, J.-H., Yoon, S.-R. & Choi, I. (2006). *J. Dermatol.* **33**, 662–669.

Chutkow, W. A., Patwari, P., Yoshioka, J. & Lee, R. T. (2008). *J. Biol. Chem.* **283**, 2397–2406.

Cnop, M., Welsh, N., Jonas, J. C., Jorns, A., Lenzen, S. & Eizirik, D. L. (2005). *Diabetes*, **54**, Suppl. 2, S97–S107.

Collins, B. M., Norwood, S. J., Kerr, M. C., Mahony, D., Seaman, M. N., Teasdale, R. D. & Owen, D. J. (2008). *Traffic*, **9**, 366–379.

Derewenda, Z. S. (2004). *Structure*, **12**, 529–535.

Emsley, P., Lohkamp, B., Scott, W. G. & Cowtan, K. (2010). *Acta Cryst.* D**66**, 486–501.

Goldberg, S. F., Miele, M. E., Hatta, N., Takata, M., Paquette-Straub, C., Freedman, L. P. & Welch, D. R. (2003). *Cancer Res.* **63**, 432–440.

Gurevich, V. V. & Gurevich, E. V. (2006). *Pharmacol. Ther.* **110**, 465–502.

Gurevich, V. V., Gurevich, E. V. & Cleghorn, W. M. (2008). *Handb. Exp. Pharmacol.*, pp. 15–37.

Han, M., Gurevich, V. V., Vishnivetskiy, S. A., Sigler, P. B. & Schubert, C. (2001). *Structure*, **9**, 869–880.

Han, S. H., Jeon, J. H., Ju, H. R., Jung, U., Kim, K. Y., Yoo, H. S., Lee, Y. H., Song, K. S., Hwang, H. M., Na, Y. S., Yang, Y., Lee, K. N. & Choi, I. (2003). *Oncogene*, **22**, 4035–4046.

Hirsch, J. A., Schubert, C., Gurevich, V. V. & Sigler, P. B. (1999). *Cell*, **97**, 257–269.

Hui, T. Y., Sheth, S. S., Diffley, J. M., Potter, D. W., Lusis, A. J., Attie, A. D. & Davis, R. A. (2004). *J. Biol. Chem.* **279**, 24387–24393.

Jeon, J.-H., Lee, K.-N., Hwang, C. Y., Kwon, K.-S., You, K.-H. & Choi, I. (2005). *Cancer Res.* **65**, 4485–4489.

Junn, E., Han, S. H., Im, J. Y., Yang, Y., Cho, E. W., Um, H. D., Kim, D. K., Lee, K. W., Han, P. L., Rhee, S. G. & Choi, I. (2000). *J. Immunol.* **164**, 6287–6295.

Kaimul, A. M., Nakamura, H., Masutani, H. & Yodoi, J. (2007). *Free Radic. Biol. Med.* **43**, 861–868.

Kim, S. Y., Suh, H.-W., Chung, J. W., Yoon, S. R. & Choi, I. (2007). *Cell. Mol. Immunol.* **4**, 345–351.

Kobayashi, T., Uehara, S., Ikeda, T., Itadani, H. & Kotani, H. (2003). *Kidney Int.* **64**, 1632–1642.

Kristiansen, O. P. & Mandrup-Poulsen, T. (2005). *Diabetes*, **54**, Suppl. 2, S114–S124.

Le Jan, S., Le Meur, N., Cazes, A., Philippe, J., Le Cunff, M., Leger, J., Corvol, P. & Germain, S. (2006). *FEBS Lett.* **580**, 3395–3400.

Lefkowitz, R. J. & Shenoy, S. K. (2005). *Science*, **308**, 512–517.

Leslie, A. G. W. (1992). *Jnt CCP4/ESF–EACBM Newsl. Protein Crystallogr.* **26**.

Marti-Renom, M. A., Stuart, A. C., Fiser, A., Sanchez, R., Melo, F. & Sali, A. (2000). *Annu. Rev. Biophys. Biomol. Struct.* **29**, 291–325.

Masutani, H., Yoshihara, E., Masaki, S., Chen, Z. & Yodoi, J. (2012). *J. Clin. Biochem. Nutr.* **50**, 23–34.

McNicholas, S., Potterton, E., Wilson, K. S. & Noble, M. E. M. (2011). *Acta Cryst.* D**67**, 386–394.

McPhillips, T. M., McPhillips, S. E., Chiu, H.-J., Cohen, A. E., Deacon, A. M., Ellis, P. J., Garman, E., Gonzalez, A., Sauter, N. K., Phizackerley, R. P., Soltis, S. M. & Kuhn, P. (2002). *J. Synchrotron Rad.* **9**, 401–406.

Milano, S. K., Kim, Y.-M., Stefano, F. P., Benovic, J. L. & Brenner, C. (2006). *J. Biol. Chem.* **281**, 9812–9823.

Minn, A. H., Hafele, C. & Shalev, A. (2005). *Endocrinology*, **146**, 2397–2405.

Moont, G., Gabb, H. A. & Sternberg, M. J. (1999). *Proteins*, **35**, 364–373.

Murshudov, G. N., Skubák, P., Lebedev, A. A., Pannu, N. S., Steiner, R. A., Nicholls, R. A., Winn, M. D., Long, F. & Vagin, A. A. (2011). *Acta Cryst.* D**67**, 355–367.

Nishinaka, Y., Nishiyama, A., Masutani, H., Oka, S., Ahsan, K. M., Nakayama, Y., Ishii, Y., Nakamura, H., Maeda, M. & Yodoi, J. (2004). *Cancer Res.* **64**, 1287–1292.

Nishiyama, A., Matsui, M., Iwata, S., Hirota, K., Masutani, H., Nakamura, H., Takagi, Y., Sono, H., Gon, Y. & Yodoi, J. (1999). *J. Biol. Chem.* **274**, 21645–21650.

Nishizawa, K., Nishiyama, H., Matsui, Y., Kobayashi, T., Saito, R., Kotani, H., Masutani, H., Oishi, S., Toda, Y., Fujii, N., Yodoi, J. & Ogawa, O. (2011). *Carcinogenesis*, **32**, 1459–1466.

Oka, S., Yoshihara, E., Bizen-Abe, A., Liu, W., Watanabe, M., Yodoi, J. & Masutani, H. (2009). *Endocrinology*, **150**, 1225–1234.
Patwari, P., Chutkow, W. A., Cummings, K., Verstraeten, V. L., Lammerding, J., Schreiter, E. R. & Lee, R. T. (2009). *J. Biol. Chem.* **284**, 24996–25003.
Patwari, P., Emilsson, V., Schadt, E. E., Chutkow, W. A., Lee, S., Marsili, A., Zhang, Y., Dobrin, R., Cohen, D. E., Larsen, P. R., Zavacki, A. M., Fong, L. G., Young, S. G. & Lee, R. T. (2011). *Cell Metab.* **14**, 671–683.
Patwari, P., Higgins, L. J., Chutkow, W. A., Yoshioka, J. & Lee, R. T. (2006). *J. Biol. Chem.* **281**, 21884–21891.
Patwari, P. & Lee, R. T. (2012). *Trends Endocrinol. Metab.* **23**, 216–222.
Peterson, C. W. & Ayer, D. E. (2011). *Front. Biosci.* **16**, 2206–2223.
Piao, Z. H. *et al.* (2009). *Cell. Mol. Biol. (Noisy-le-grand)*, **55**, Suppl., OL1096–OL1103.
Polekhina, G., Ascher, D. B., Kok, S. F. & Waltham, M. (2011). *Acta Cryst.* F**67**, 613–617.
Powis, G. & Montfort, W. R. (2001). *Annu. Rev. Biophys. Biomol. Struct.* **30**, 421–455.
Qi, W., Chen, X., Gilbert, R. E., Zhang, Y., Waltham, M., Schache, M., Kelly, D. J. & Pollock, C. A. (2007). *Am. J. Pathol.* **171**, 744–754.
Qi, W., Chen, X., Holian, J., Tan, C. Y. R., Kelly, D. J. & Pollock, C. A. (2009). *Am. J. Pathol.* **175**, 1858–1867.
Schubert, C., Hirsch, J. A., Gurevich, V. V., Engelman, D. M., Sigler, P. B. & Fleming, K. G. (1999). *J. Biol. Chem.* **274**, 21186–21190.
Schulz, E., Anter, E. & Keaney, J. F. Jr (2004). *Curr. Med. Chem.* **11**, 1093–1104.
Schulze, P. C., Yoshioka, J., Takahashi, T., He, Z., King, G. L. & Lee, R. T. (2004). *J. Biol. Chem.* **279**, 30369–30374.
Shalev, A. (2008). *Biochem. Soc. Trans.* **36**, 963–965.
Shi, H., Rojas, R., Bonifacino, J. S. & Hurley, J. H. (2006). *Nature Struct. Mol. Biol.* **13**, 540–548.
Shin, D., Jeon, J.-H., Jeong, M., Suh, H.-W., Kim, S., Kim, H.-C., Moon, O.-S., Kim, Y.-S., Chung, J. W., Yoon, S. R., Kim, W.-H. & Choi, I. (2008). *Biochim. Biophys. Acta*, **1783**, 838–848.
Spindel, O. N., World, C. & Berk, B. C. (2012). *Antioxid. Redox Signal.* **16**, 587–596.
Sutton, R. B., Vishnivetskiy, S. A., Robert, J., Hanson, S. M., Raman, D., Knox, B. E., Kono, M., Navarro, J. & Gurevich, V. V. (2005). *J. Mol. Biol.* **354**, 1069–1080.
Vagin, A. & Teplyakov, A. (2010). *Acta Cryst.* D**66**, 22–25.
Van Duyne, G. D., Standaert, R. F., Karplus, P. A., Schreiber, S. L. & Clardy, J. (1993). *J. Mol. Biol.* **229**, 105–124.
Wassmann, S., Wassmann, K. & Nickenig, G. (2004). *Hypertension*, **44**, 381–386.
Watanabe, R., Nakamura, H., Masutani, H. & Yodoi, J. (2010). *Pharmacol. Ther.* **127**, 261–270.
Winn, M. D. *et al.* (2011). *Acta Cryst.* D**67**, 235–242.
Xiang, G., Seki, T., Schuster, M. D., Witkowski, P., Boyle, A. J., See, F., Martens, T. P., Kocher, A., Sondermeijer, H., Krum, H. & Itescu, S. (2005). *J. Biol. Chem.* **280**, 39394–39402.
Zhan, X., Gimenez, L. E., Gurevich, V. V. & Spiller, B. W. (2011). *J. Mol. Biol.* **406**, 467–478.
Zhou, R., Tardivel, A., Thorens, B., Choi, I. & Tschopp, J. (2010). *Nature Immunol.* **11**, 136–140.